7-3-2023

Age-related alterations in meningeal immunity drive impaired CNS lymphatic drainage

Justin Rustenhoven
Washington University School of Medicine in St. Louis

Georgios Pavlou
Massachusetts Institute of Technology

Steffen E Storck
Washington University School of Medicine in St. Louis

Taitea Dykstra
Washington University School of Medicine in St. Louis

Siling Du
Washington University School of Medicine in St. Louis

See next page for additional authors

Follow this and additional works at: https://digitalcommons.wustl.edu/oa_4

Part of the Medicine and Health Sciences Commons

Please let us know how this document benefits you.

Authors

Justin Rustenhoven, Georgios Pavlou, Steffen E Storck, Taitea Dykstra, Siling Du, Zhengpeng Wan, Daniel Quintero, Joshua P Scallan, Igor Smirnov, Roger D Kamm, and Jonathan Kipnis

BRIEF DEFINITIVE REPORT

Age-related alterations in meningeal immunity drive impaired CNS lymphatic drainage

Justin Rustenhoven[1,2,3,4], Georgios Pavlou[5*], Steffen E. Storck[1,2*], Taitea Dykstra[1,2], Siling Du[1,2,6], Zhengpeng Wan[5], Daniel Quintero[1,2], Joshua P. Scallan[7], Igor Smirnov[1,2], Roger D. Kamm[5,8], and Jonathan Kipnis[1,2,6]

The meningeal lymphatic network enables the drainage of cerebrospinal fluid (CSF) and facilitates the removal of central nervous system (CNS) waste. During aging and in Alzheimer's disease, impaired meningeal lymphatic drainage promotes the buildup of toxic misfolded proteins in the CNS. Reversing this age-related dysfunction represents a promising strategy to augment CNS waste clearance; however, the mechanisms underlying this decline remain elusive. Here, we demonstrate that age-related alterations in meningeal immunity underlie this lymphatic impairment. Single-cell RNA sequencing of meningeal lymphatic endothelial cells from aged mice revealed their response to IFNγ, which was increased in the aged meninges due to T cell accumulation. Chronic elevation of meningeal IFNγ in young mice via AAV-mediated overexpression attenuated CSF drainage—comparable to the deficits observed in aged mice. Therapeutically, IFNγ neutralization alleviated age-related impairments in meningeal lymphatic function. These data suggest manipulation of meningeal immunity as a viable approach to normalize CSF drainage and alleviate the neurological deficits associated with impaired waste removal.

Introduction

Many neurodegenerative diseases are associated with a failure to clear misfolded proteins promoting their accumulation in the central nervous system (CNS), neuronal dysfunction, and cognitive deficits (Boland et al., 2018; Zlokovic, 2005). In peripheral tissues, such matter is typically cleared via tissue-resident lymphatic networks that drain interstitial fluid (ISF), enabling waste removal and immune surveillance (Oliver et al., 2020). While the brain parenchyma lacks lymphatic vasculature, this network exists in the meninges, triple-layered membranes that surround the CNS (Absinta et al., 2017; Aspelund et al., 2015; Louveau et al., 2015). By flushing the ISF out of the brain into the cerebrospinal fluid (CSF)—termed the "glymphatic" system—tissue waste is continuously exchanged with the CSF (Iliff et al., 2012). This waste is subsequently effluxed to the dura where it can be drained via a lymphatic network into deep and superficial cervical lymph nodes, thus enabling CNS waste removal (Rustenhoven et al., 2021; Louveau et al., 2018; Ringstad and Eide, 2020; Ahn et al., 2019).

Aging is the major risk factor for the development of late-onset sporadic neurodegenerative diseases, including

Alzheimer's disease (AD) and Parkinson's disease, both of which display pathological protein accumulation in the CNS that is believed to contribute to neuronal death (Boland et al., 2018; Hou et al., 2019). Critically, meningeal lymphatic function is significantly perturbed during aging, resulting in a failure of CSF drainage (Ahn et al., 2019; Da Mesquita et al., 2018). This deficit in lymphatics is less pronounced in other peripheral tissues including the skin, trachea, and diaphragm, suggesting a unique sensitivity of the meningeal lymphatic network in age-related decline (Ahn et al., 2019).

The meningeal lymphatic network draining CSF is situated almost exclusively flanking large vascular structures in the meninges, called the dural sinuses (Absinta et al., 2017; Louveau et al., 2015; Antila et al., 2017). We recently identified the dural sinuses as highly orchestrated immunological hubs that selectively permit T cell trafficking through a specialized stromal niche (Rustenhoven et al., 2021). These sites also preferentially enable CSF access into the dural meninges for subsequent lymphatic drainage (Rustenhoven et al., 2021). During aging, the

[1]Brain Immunology and Glia Center, School of Medicine, Washington University in St. Louis, St. Louis, MO, USA; [2]Department of Pathology and Immunology, School of Medicine, Washington University in St. Louis, St. Louis, MO, USA; [3]Department of Pharmacology and Clinical Pharmacology, The University of Auckland, Auckland, New Zealand; [4]Centre for Brain Research, The University of Auckland, Auckland, New Zealand; [5]Department of Biological Engineering, Massachusetts Institute of Technology, Cambridge, MA, USA; [6]Immunology Graduate Program, School of Medicine, Washington University in St. Louis, St. Louis, MO, USA; [7]Department of Molecular Pharmacology and Physiology, University of South Florida, Tampa, FL, USA; [8]Department of Mechanical Engineering, Massachusetts Institute of Technology, Cambridge, MA, USA.

*G. Pavlou and S.E. Storck contributed equally to this paper. Correspondence to Jonathan Kipnis: kipnis@wustl.edu; Justin Rustenhoven: justin.rustenhoven@auckland.ac.nz.

stromal composition of the dural sinuses is altered, resulting in elevated leukocyte adhesion molecules and deposition of T cell–retention factors, which coincided with substantial immune cell alterations, particularly T cell accumulation (Rustenhoven et al., 2021). These T cells can secrete various cytokines, including IL-4, IL-17, and IFNγ that, under homeostasis, contribute to homeostatic CNS functions through direct neuronal signaling (Alves de Lima et al., 2020a; Salvador et al., 2021; Herz et al., 2021; Filiano et al., 2016). However, such T cell–derived cytokines—particularly in elevated states following pathologies—may also contribute to impaired lymphatic function (Shin et al., 2015; Kataru et al., 2011).

Improving lymphatic drainage may have significant benefits in promoting the clearance of misfolded, disease-related proteins in age-related neurodegenerative disease, including amyloid β (Aβ) and tau in AD (Da Mesquita et al., 2018, 2021; Patel et al., 2019), and α synuclein in Parkinson's disease (Ding et al., 2021; Zou et al., 2019). Surprisingly, the cause of this age-related meningeal lymphatic decline remains largely unexplored. Identifying factors that promote their decline, and indeed mechanisms to reverse this could enable the development of attractive therapeutic interventions. Here, we identify an age-related meningeal lymphatic signature characterized by responsiveness to IFNγ signaling. We demonstrate that aging results in elevated meningeal IFNγ expression driven by CD4 and CD8 T cells, that this signaling axis directly impairs lymphatic function, and that neutralization of IFNγ in aged mice alleviates age-related meningeal lymphatic dysfunction.

Results and discussion

Aging is associated with a decline in meningeal lymphatic function, resulting in attenuated drainage of CSF to deep cervical lymph nodes (dCLNs; Ahn et al., 2019; Da Mesquita et al., 2018). However, the mechanisms responsible for this decline remain elusive. To determine potential mediators underlying age-related meningeal lymphatic dysfunction in a non-bias screen, we performed deep (1 million reads/cell) single-cell sequencing of FACS-enriched viable CD45⁻ PDPN⁺ LYVE1⁺ CD31⁺ lymphatic endothelial cells (LECs) from the dura of young and aged mice (Fig. 1 A). t-distributed stochastic neighbor embedding (t-SNE) dimensionality reduction and visualization of 357 LECs from young and aged mice demonstrated segregation by age (Fig. 1 B). Analysis of differentially expressed genes (DEGs) in LECs isolated from young and aged mice and their associated biological processes by gene ontology (GO) demonstrated a strong age-related induction of pathways related to antigen presentation and cellular responsiveness to IFNγ signaling (Fig. 1, C and D). Importantly, we also observed the presence of *Ifngr1* and *Ifngr2* on LECs, demonstrating their ability to directly respond to IFNγ signaling (Fig. 1 E).

The dural meninges, unlike the brain parenchyma, host a rich repertoire of immune cells (Rustenhoven et al., 2021; Mrdjen et al., 2018; Van Hove et al., 2019). Under steady-state conditions, T cells situated in the dura—closely associated with meningeal lymphatic vasculature—produce cytokines that regulate mouse behavior through direct neuronal signaling

(Salvador et al., 2021; Alves de Lima et al., 2020b). During aging, the dural meninges display a significant expansion of both CD4 and CD8 T cells (Fig. 1, F–H), yet these retain relatively comparable polarization status with respect to *Tbx21* (Th1), *Gata3* (Th2), *Rorc* (Th17), and *Foxp3* (regulatory T cell) phenotypes (Fig. S1, A–E). Th1-polarized T cells are major producers of IFNγ, which we previously demonstrated to signal on aged LECs (Fig. 1 G). To investigate whether this age-related IFNγ response in LECs could be attributed to elevated expression by conventional T cells, we utilized intracellular flow cytometry and confirmed an increased frequency of IFNγ-producing CD4 and CD8 T cells in the aged dura (Fig. 1, I–L). To determine whether this cytokine-producing capacity translated to elevated production in the aged dura, we utilized Luminex analysis of mouse dural homogenates and demonstrated a significant increase in IFNγ protein in the meninges of aged mice compared with their young counterparts (Fig. 1 M).

These data suggested that IFNγ secretion by CD4 and CD8 T cells may signal onto nearby meningeal LECs and contribute to the age-related dysfunction in CSF drainage. To explore this hypothesis mechanistically, we generated adeno-associated virus (AAV) 9-CMV viruses expressing GFP or IFNγ and administered these to the CSF via intra-cisterna magna (i.c.m.) injections into young 8-wk-old mice. 1 mo after viral transduction, this experimental paradigm resulted in efficient overexpression of IFNγ in the dura of young mice as confirmed by Luminex analysis of dural homogenates (Fig. 2 A). Examination of i.c.m. delivered ovalbumin-Alexa Fluor 594 (OVA-594) drainage to dCLNs was significantly perturbed with IFNγ overexpression (Fig. 2, B–D), reflecting the functional impairment observed in aged mice (Ahn et al., 2019; Da Mesquita et al., 2018). Importantly, efflux of OVA-594 to the dura was unchanged with IFNγ overexpression (Fig. 2, E–G), in agreement with our previous results that meningeal lymphatic function does not alter access of CSF to this tissue (Rustenhoven et al., 2021). In addition to a decline in meningeal lymphatic function, OVA-594 infiltration into the brain parenchyma (glymphatic influx) was also reduced, as previously described for aged mice, and that was mechanistically linked with impaired lymphatic function (Da Mesquita et al., 2018; Kress et al., 2014; Benveniste et al., 2019; Fig. S1, F and G). Importantly, this pathway facilitates the removal of brain waste into the CSF, and thus, together with the lymphatic system, forms an essential component of CNS clearance (Louveau et al., 2017).

To examine potential mechanisms underlying IFNγ-driven lymphatic dysfunction, we performed RNA sequencing (RNA-seq) of in vitro cultures of mouse dermal LECs following a semichronic 72-h treatment with IFNγ. Examining the GO pathways associated with downregulated genes, we noted transcriptomic changes relating to the extracellular matrix organization, vascular development, and cell–cell junctions (Fig. S3, A–D). Using the upregulated transcripts to generate an IFNγ response signature, we also noted a significant enhancement of this signature score on our LECs isolated from the aged meninges (Fig. S3 E). Importantly, alterations in adherans junctions in meningeal lymphatic vessels were previously observed in aged mice (Ahn et al., 2019), and appropriate
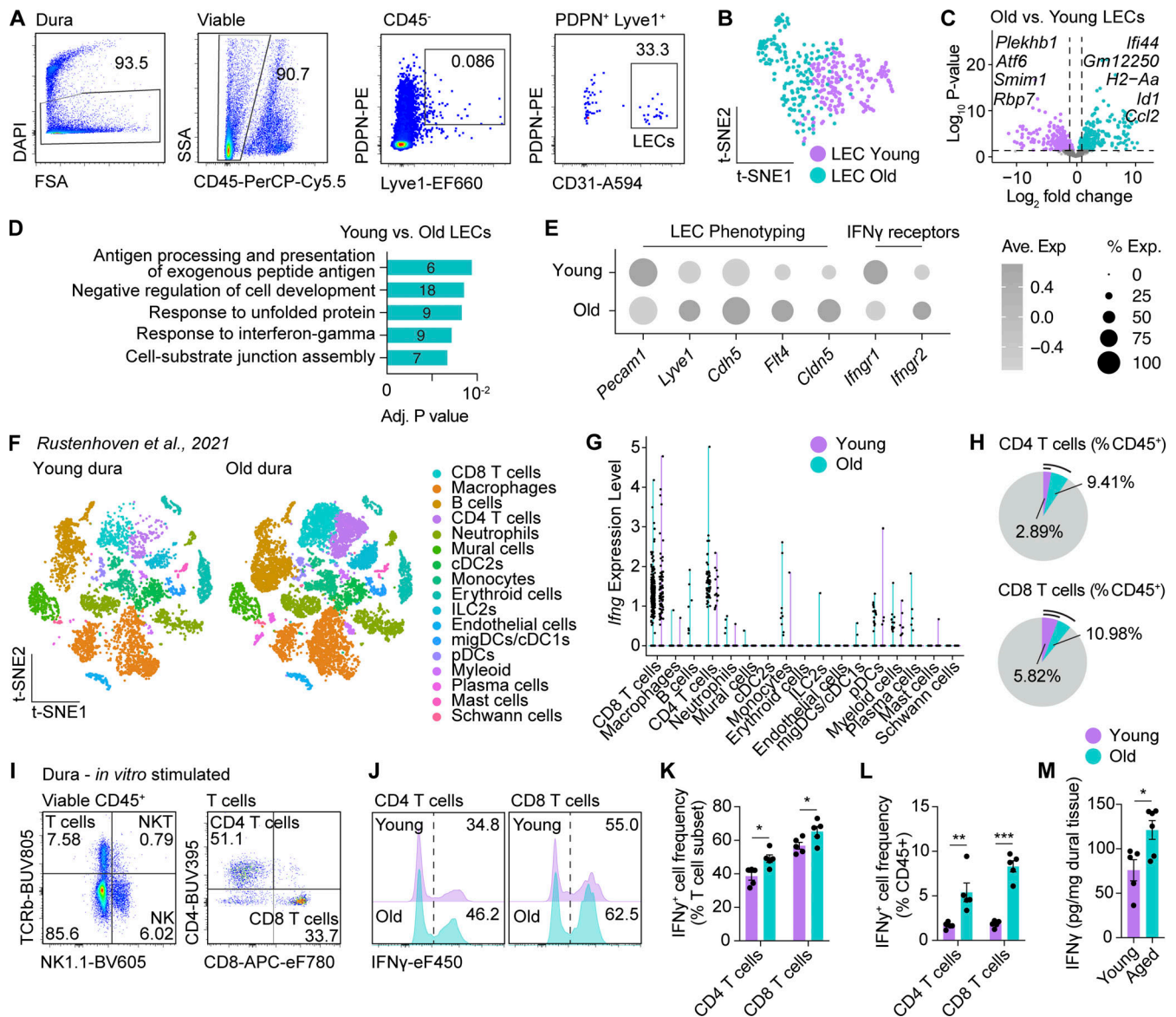
Figure 1. **Age-related changes in meningeal lymphatics implicate T cell–derived IFNγ signaling in their dysfunction. (A)** Flow cytometry gating strategy for the isolation of dural meningeal LECs. Numbers on flow plots represent the frequency (%) of the gated population. **(B)** t-SNE visualization of scRNA-seq analysis of LECs isolated from the dura of young (2–3 mo) and aged (20–24 mo) mice; $n = 5$ individual young and old dura per experiment, $n = 2$ independent experiments, 10 dura samples per age total. **(C)** Volcano plot demonstrating DEGs between young and aged dural LECs. **(D)** GO pathway analysis demonstrating enriched pathways upregulated in aged LECs. Numbers represent the number of genes in respective pathways. **(E)** Dot-plot showing expression of LEC phenotyping markers and receptors for IFNγ. **(F)** t-SNE visualization of scRNA-seq of cells isolated from young (2–3 mo) and aged (20–24 mo) mouse dura. Data are from Rustenhoven et al. (2021); $n = 5$ individual young and old dura per experiment, $n = 2$ independent experiments, 10 dura samples per age total. **(G)** Violin plot demonstrating *Ifng* gene expression in meningeal cells of young and aged mice. **(H)** Pie chart demonstrating CD4^{+} and CD8^{+} T cells as a percentage of all CD45^{+} cells in young and aged mice from sequencing analysis. **(I–L)** Flow cytometry gating strategy and quantification of IFNγ^{+} CD4^{+} or CD8^{+} T cells isolated from young and aged dura following in vitro stimulation for 6 h with PMA/ionomycin and brefeldin A, expressed as a percentage of specific T cell subsets or percentage of total CD45^{+} cell frequency. *, $P < 0.05$; **, $P < 0.01$; ***, $P < 0.001$ (two way-ANOVA with Sidak's post-hoc test), $n = 5$ individual mice per experiment, representative of two independent experiments. Numbers on flow plots represent the frequency (%) of the gated population. **(M)** Luminex analysis of IFNγ concentrations in dural homogenates from young and aged mice. *, $P < 0.05$ (Student's t test), $n = 5–6$ individual mice per experiment, representative of two independent experiments.

maintenance of such junctions is critical to permit functional lymphatic drainage (Hägerling et al., 2018; Jannaway and Scallan, 2021; Yang et al., 2019). To examine whether IFNγ signaling on LECs could directly impair lymphatic endothelial junctions, we utilized in vitro cultures of mouse dermal LECs. Following a semichronic 72-h treatment with IFNγ, we observed

significant mislocalization of VE-Cadherin—a critical mediator of LEC adherans junctions—from its prototypical cell–cell junction expression and a significant enhancement in gaps between cells (Fig. 2, H and I). Mechanistically, such an alteration in VE-Cadherin junction expression would lead to lymphatic hyperpermeability at the collecting level and impair drainage of

Rustenhoven et al.
Aged meningeal immunity drives lymphatic impairments

Journal of Experimental Medicine 3 of 12
https://doi.org/10.1084/jem.20221929
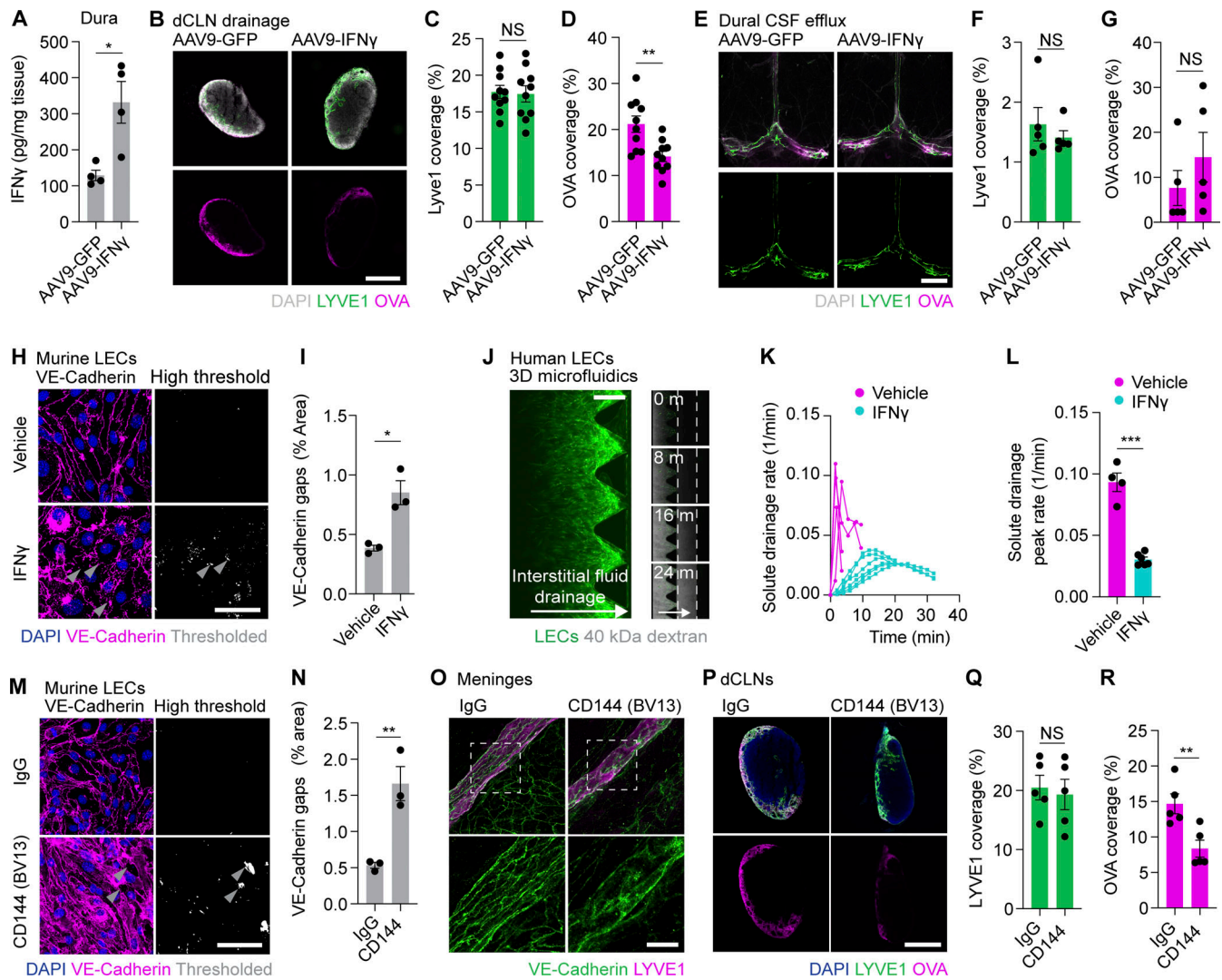
Figure 2. **IFNγ drives meningeal lymphatic junctional disruption and impairs drainage of CSF. (A)** Luminex analysis for IFNγ concentrations in dural homogenates of 3-mo-old mice that received an i.c.m. injection of 2 µl of 1×10^{13} GC of AAV9-CCMV-GFP or AAV9-CCMV-IFNγ at 2 mo of age. *, P < 0.05 (Student's t test), n = 4 individual mice per experiment, representative of n = 3 independent experiments. **(B–G)** Immunohistochemistry and quantification of LYVE1^{+} lymphatic vasculature and OVA-594 coverage in the (B–D) CSF-draining dCLNs or (E–G) the dural meninges in mice that received an i.c.m. injection of 2 µl of 1×10^{13} GC of AAV9-CCMV-GFP or AAV9-CCMV-IFNγ at 2 mo of age, and an i.c.m. injection of 2.5 µl OVA-594 (1 µg/µl) 1 h prior to sacrifice at 3 mo of age. **, P < 0.01 (Student's t test), n = 5–10 individual mice per experiment, representative of n = 2 independent experiments. Scale bar = 300 µm (B) or 2 mm (E). **(H)** Immunocytochemistry of VE-Cadherin in C57BL/6 mouse primary dermal LECs treated for 24 h every 72 h with 5 ng/ml IFNγ or a vehicle control. Scale bar = 50 µm. **(I)** Quantification of VE-Cadherin gaps between adjacent cells after application of a high threshold imaging parameter. *, P < 0.05 (Student's t test), n = 3 independent experiments. **(J)** Live imaging snapshots of 40 kD Texas Red dextran drainage in 3D microfluidic devices with human LECs cultured in 3D fibrin matrices on-chip to form luminized vessels. Scale bar = 400 µm. **(K and L)** Quantification of solute drainage rate over time and peak solute drainage rate achieved in LECs treated with 2 U/ml IFNγ or a vehicle control 24 h prior to application of 40 kD Texas Red dextran. ***, P < 0.001 (Student's t test), n = 4–6 individual devices per experiment, representative of n = 2 independent experiments. **(M)** Immunocytochemistry of VE-Cadherin in C57BL/6 mouse primary dermal LECs treated for 6 h with 50 µg/ml of a CD144/VE-Cadherin antibody (BV13) or IgG isotype control. Scale bar = 50 µm. **(N)** Quantification of VE-Cadherin gaps between adjacent cells after application of a high threshold imaging parameter. **, P < 0.01 (Student's t test), n = 3 independent experiments. **(O)** Immunohistochemistry of VE-Cadherin distribution in lymphatic dural vasculature in 2-mo-old mice that received an i.c.m. injection of 2.5 µg anti-CD144 or IgG isotype (0.5 µg/µl) 7 h prior to sacrifice, representative of n = 2 independent experiments. Scale bar = 20 µm. **(P–R)** Immunohistochemistry and quantification of LYVE1^{+} lymphatic vasculature and OVA-594 coverage in 2-mo-old mice that received an i.c.m. injection of 2.5 µg anti-CD144 or IgG isotype (0.5 µg/µl) 7 h prior to sacrifice and an i.c.m. injection of 2.5 µg OVA-594 (1 µg/µl) 1 h prior to sacrifice. **, P < 0.01 (Student's t test), n = 5 individual mice per experiment, representative of n = 2 independent experiments. Scale bar = 300 µm.

ISF (Hägerling et al., 2018; Jannaway and Scallan, 2021; Yang et al., 2019).

Alternative lymphatic alterations, including valve disruption, or lymphatic zippering could also contribute to impaired CSF drainage. Recently, a VEGF-A mediated zippering of dermal

lymphatic junctions—a functional shift from button junctions to zipper junctions—was described that prevents viral dissemination through the body (Churchill et al., 2022). To explore whether this could contribute to our observed meningeal phenotypes, we explored VEGF-A–producing cells in our young and

Rustenhoven et al.
Aged meningeal immunity drives lymphatic impairments

Journal of Experimental Medicine   4 of 12
https://doi.org/10.1084/jem.20221929

aged single-cell RNA-seq (scRNA-seq) dataset. While a significant induction in VEGF-A–producing mast cells and plasma cells was observed with aging (Fig. S2, A–C), we did not observe evidence for VEGF-A/VEGFR2 signaling on aged meningeal lymphatics that would drive a zippering phenotype (Fig. S2, D and E). This is consistent with the shift toward button junctions previously observed in aged meningeal lymphatics (Ahn et al., 2019). Additionally, using three-dimensional (3D) microfluidic models incorporating luminized human lymphatic vasculature and physiological hydrodynamic flow (Fig. S3, F–H), we found that IFNγ directly impaired drainage of 40 kD Texas Red dextran (Fig. 2, J–L) and disrupted VE-Cadherin junctions (Fig. S3 I), suggesting that IFNγ can directly impair lymphatic function without the need for any intermediate cell types.

To determine whether altered VE-Cadherin expression was sufficient to explain the impaired lymphatic function observed in aged mice, we utilized a specific VE-Cadherin clone (BV13) that disrupts VE-Cadherin membrane localization (Corada et al., 1999; Jannaway and Scallan, 2021). Using in vitro cultures, we confirmed the disruption of VE-Cadherin membrane polarization in LECs after a 6 h treatment with the BV13 clone (Fig. 2, M and N). We then queried whether direct disruption of VE-Cadherin in vivo could recapitulate the IFNγ-induced lymphatic impairment. CSF delivery of the BV13 antibody via an i.c.m. injection resulted in impaired VE-Cadherin polarization in LECs in the dura matter (Fig. 2 O) and attenuated lymphatic drainage of OVA-594 to dCLNs, mechanistically linking altered VE-Cadherin with impaired drainage (Fig. 2, P–R). This acute administration of BV13 antibodies would be expected to disrupt lymphatic junctions, but not valves, arguing against the requirement for lymphatic valve dysfunction to drive impaired CSF drainage. However, this does not rule out additional long-term mediated valve disruption by aged meningeal immunity as an additional contributing factor. Collectively, these data suggest that IFNγ signaling directly on meningeal lymphatics can drive altered VE-Cadherin expression, resulting in impaired lymphatic function in aging.

Given our data implicating IFNγ in impairing lymphatic drainage of CSF, we investigated whether its neutralization in aged mice could improve lymphatic function. Aged mice received i.p. injections of anti-IFNγ neutralizing antibodies or IgG isotype control every 72 h for 8 wk after which we assessed lymphatic drainage (Fig. 3 A). While no change in lymphatic coverage was observed in aged mice or indeed "glymphatic" influx of CSF-delivered ovalbumin (Fig. S3, J and K), we saw markedly improved lymphatic drainage of OVA-594 to dCLNs (Fig. 3, B–D). These data suggest that peripheral neutralization of IFNγ represents a feasible therapeutic target in alleviating age-related lymphatic dysfunction, without necessarily impacting other brain clearance systems. Importantly, it also demonstrates that age-related meningeal lymphatic decline is reversible, highlighting the potential for clinical translation of these findings for aged or late-stage neurodegenerative disease patients.

While the development of neurodegenerative diseases such as AD is multifactorial, improving lymphatic drainage may have significant benefits in promoting appropriate clearance of Aβ and tau that are present in the CNS and CSF of AD patients, and
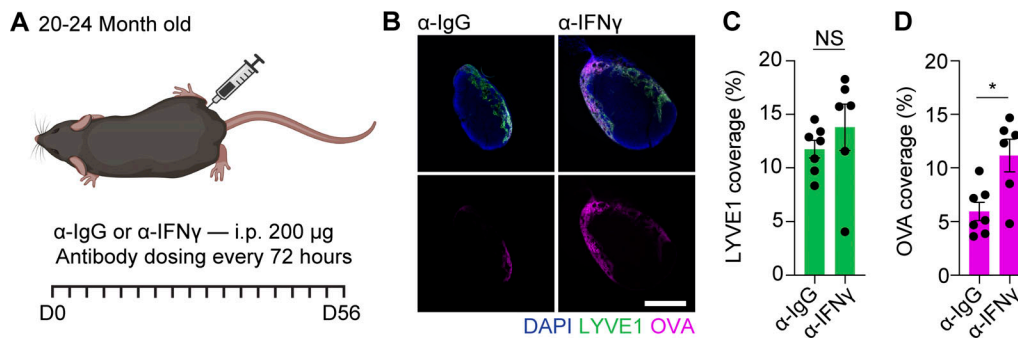
can be found in CSF-draining lymph nodes (Da Mesquita et al., 2018, 2021; Patel et al., 2019). Further, the effectiveness of anti-amyloid immunotherapy with aducanumab is coupled to the functional state of the meningeal lymphatic drainage (Da Mesquita et al., 2021), and therefore interventions that promote meningeal lymphatic function may further augment pre-existing therapeutics. Surprisingly, the cause of meningeal lymphatic decline that occurs in aging has been largely unexplored, thus, mechanisms to alleviate this dysfunction remained elusive. Our observation of an age-related meningeal lymphatic IFNγ response signature that impairs CSF drainage represents a novel therapeutic avenue to alleviate their decline. While sustained IFNγ neutralization is unlikely to represent a direct therapeutic approach, due to the possibility of opportunistic pathogen infections or tumor formation, targeting components of the meningeal immune cell repertoire are feasible. Intrathecal administrations in humans allows direct targeting of tissues reached by CSF, and we previously demonstrated we can specifically manipulate meningeal T cells via such an approach (Alves de Lima et al., 2020a). Additionally, transcranial delivery of small molecules through the cranium has proved effective in limiting neuroinflammatory responses in the CNS borders and reaches the dural mater (Roth et al., 2014). Additionally, unlike the brain or leptomeningeal vasculature, the dural sinuses which neighbor the meningeal lymphatic network are highly permeable and do not possess blood–brain barrier properties that limit drug accessibility, allowing easy access to systemically delivered therapeutics (Rustenhoven et al., 2021).

Beyond implications for aging, an appreciation of factors contributing to meningeal lymphatic decline may be valuable in understanding the pathology of diverse neurodegenerative diseases. We anticipate that the immune-driven impairments identified here will be broadly applicable to other neurodegenerative diseases with inflammatory components—including AD and Parkinson's disease—and may represent an attractive therapeutic approach to improve misfolded protein removal.

Materials and methods
Animals
Male or female wild-type mice (C57BL/6J background) were bred in-house and purchased from the Jackson Laboratory (JAX000664; WT) or provided by the National Institute of Health/National Institute of Aging. All mice were wild-type, and thus no backcrossing was performed. All mice were habituated for at least 1 wk in the animal facility before the start of experimentation. All experimental comparisons with young (2–3 mo old) mice were made using littermate controls. Aged mice (20–24 mo old) were received from the National Institute of Health/National Institute of Aging and compared to young mice bred in-house, as described previously. Mice were housed in a temperature- and humidity-controlled environment with a 12 h light/dark cycle (7:00 am–7:00 pm) and were provided with regular rodent chow and sterilized water ad libitum. Unless stated otherwise, mice were tested at 2–3 mo of age (young mice) or 20–24 mo of age (old mice). Sample sizes were chosen on the basis of a power analysis using estimates from previously

Rustenhoven et al.
Aged meningeal immunity drives lymphatic impairments

Journal of Experimental Medicine   5 of 12
https://doi.org/10.1084/jem.20221929

Figure 3. IFNγ neutralization improves meningeal lymphatic drainage in aged mice. (A) Schematic for the experimental paradigm of IFNγ neutralization in aged (20–24 mo old) mice. **(B–D)** Immunohistochemistry and quantification of LYVE1⁺ lymphatic vasculature and OVA-594 coverage in CSF-draining dCLNs of aged mice that received i.p. injections of 200 µg anti-IgG or anti-IFNγ every 72 h for 8 wk and an i.c.m. injection of 2.5 µl OVA-594 (1 µg/µl) 1 h prior to sacrifice. *, P < 0.05 (Student's *t* test), *n* = 6–7 individual mice per experiment, representative of *n* = 3 independent experiments. Scale bar = 300 µm.

published experiments. All experiments were approved by the Institutional Animal Care and Use Committee of Washington University in St. Louis.

I.c.m. injections

Ovalbumin conjugated to Alexa Fluor-594 (OVA-594; Thermo Fisher Scientific) was resuspended in sterile PBS at 1 mg/ml. Mice were anesthetized with i.p. ketamine (100 mg/ml)/xylazine (10 mg/ml). The head and neck were shaved and cleaned with iodine and 70% ethanol, and the head was mounted securely in a stereotaxic frame. A small incision in the neck was made and the muscle layers were retracted to expose the cisterna magna. Using a Hamilton syringe (coupled to a 33-gauge needle), 2.5 µl of OVA-594, 5 µl of CD144 antibody (BV13 clone, Thermo Fisher Scientific), or 5 µl of IgG control (Thermo Fisher Scientific) was injected at a rate of 1 µl/min and left in place an additional 2 min to prevent backflow. The syringe was retracted and the skin sutured closed. Mice were injected subcutaneously with 2 mg/kg ketoprofen and allowed to recover on a heat pad. Given CSF dynamics display circadian rhythmicity, injections for drainage measurements are performed in an alternating manner between different groups and harvested in the same way to ensure that no groups display an overt circadian difference. Further, we ensure that all experiments, including replications, are performed at roughly comparable times of the day to ensure that similar circadian responses will be present.

IFNγ neutralization

Aged mice (20–24 mo old) received i.p injections of 200 µg of InVivoPlus anti-mouse IFNγ (clone XMG1.2; BioXcell) or InVivoPlus rat IgG1 isotype control (clone HRPN; BioXcell) every 72 h for 8 wk.

Immunohistochemistry and analysis

Mice were given a lethal dose of anesthetics via i.p. Euthasol (10% vol/vol), and transcardial perfusion was performed with 0.025% heparin in PBS. For lymph node analysis, dCLNs were resected and tissue was drop-fixed in 4% paraformaldehyde (PFA) at 4°C for 24 h. For the vast majority of mice (>95%), a single dCLN was present on either side of the trachea so data

points almost exclusively represent pooled analysis from *n* = 2 nodes per mouse (with the exception where *n* = 3). Because lateral bias of CSF drainage can be observed, only mice where both dCLNs could be harvested were analyzed. Lymph nodes were transferred to 30% sucrose for an additional 24 h at 4°C, then embedded in optimal cutting temperature reagent (Thermo Fisher Scientific), and frozen over dry ice. Lymph nodes were cut in a cryostat (Leica CM3050 S) at 30-µm-thick sections and mounted directly onto gelatin-coated glass slides, with ~10–20 sections per slide spanning the entirety of the lymph node. Sections were marked using a hydrophobic pen and permeabilized/blocked for 30 min with PBS with 0.2% Triton-X100 (PBS-T) and 2% chicken serum (collectively termed immunobuffer) at room temperature. Sections were then incubated overnight at 4°C with gentle agitation with Lyve1-A488 (ALY7 clone; Thermo Fisher Scientific) or Lyve1-A647 (ALY7 clone; Thermo Fisher Scientific). Sections were washed, counterstained for 10 min with DAPI (1 µg/ml; Sigma-Aldrich) in PBS-T, and coverslipped with ProLong Gold (Thermo Fisher Scientific). Lymph nodes were imaged using a Leica Stellaris confocal microscope or a Slideview VS200 (Olympus) wide-field fluorescent microscope. Image analysis was performed using FIJI plugin for ImageJ (National Institutes of Health). Analysis of lymphatic drainage and Lyve1 coverage in lymph nodes was performed as described previously using thresholded OVA or Lyve1 coverage as a percentage of overall lymph node area. For each mouse, 10–20 sections were analyzed and averaged to generate the value for a single mouse.

For brains and meninges, mice were decapitated immediately posterior to the occipital bone, and overlying skin and muscle were removed from the skull. The mandibles and skull rostral to maxillae were removed and the remaining skull was drop-fixed in 4% PFA at 4°C for 24 h. The skull cap was then removed with fine surgical scissors by clockwise incisions, beginning and ending at the occipital bone, and was stored in PBS. The brain was removed, placed in 4% PFA for an additional 24 h (48 h total), then transferred to 30% sucrose in PBS until the brains had completely sunk (24–48 h). Brains were embedded in optimal cutting temperature and rapidly frozen over dry ice. Coronal cryosections 100-µm-thick were cut on a cryostat (Leica

CM3050 S), and free-floating sections were stored in PBS until use. Meningeal whole mounts were prepared by careful peeling from the skull cap using fine surgical forceps and stored in PBS. Free-floating brain sections and meningeal whole mounts were blocked and permeabilized for 1 h at room temperature in 24-well plates with constant agitation using an immunobuffer. Sections were then incubated with primary antibodies in immunobuffer at 4°C for 24 h with agitation, washed three times for 10 min each in PBS-T, and if required, incubated with secondary antibodies at room temperature for 2 h with agitation. Sections were washed once in PBS-T, incubated with DAPI in PBS-T for 10 min, and then washed in PBS-T. Sections were mounted onto glass slides and coverslipped with ProLong Gold. Sections were imaged using a Leica Stellaris confocal microscope or a Slideview VS200 (Olympus) wide-field fluorescent microscope. Image analysis was performed using FIJI plugin for ImageJ (National Institutes of Health). Analysis of glymphatic influx in brains was performed as described previously using thresholded OVA coverage as a percentage of overall brain-slice area. For each mouse, 10–20 brain sections were analyzed and averaged to generate the value for a single mouse. Analysis of meningeal Lyve1 and OVA coverage was performed as described previously using thresholded OVA or Lyve1 coverage as a percentage of the overall meningeal area.

Single-cell isolations and flow cytometry

Mice were given a lethal dose of anesthetics via i.p. Euthasol (10% vol/vol), and transcardial perfusion was performed with 0.025% heparin in PBS. For the meninges, skull caps were obtained as described in the "immunohistochemistry" procedures, and meninges were peeled from the skull cap using fine forceps and placed in ice-cold DMEM for the entirety of the collection. Meninges were then digested for 15 min at 37°C with constant agitation using 1 ml of prewarmed digestion buffer (DMEM, with 2% FBS, 1 mg/ml collagenase VIII [Sigma-Aldrich] and 0.5 mg/ml DNase I [Sigma-Aldrich]), filtered through a 70-μm cell strainer, and neutralized with 1 ml of complete medium (DMEM with 10% FBS). An additional 2 ml of FACS buffer was added, samples were centrifuged at 400 ×g for 5 min, resuspended in FACS buffer, and kept on ice. For surface staining only, samples were incubated with Zombie NIR (BioLegend) Fixable Viability Kits diluted 1:500 in PBS for 15 min at 4°C. Samples were centrifuged, resuspended in FACS buffer with anti-CD16/32 (FC block; BioLegend), diluted 1:50 in FACS buffer, and fluorescently conjugated with antibodies added for 20 min at 4°C. For surface staining only, samples were washed in FACS buffer, ran on a Cytek Aurora spectral flow cytometer (Cytek), and analyzed using FlowJo software (Tree Star). For intracellular staining of cytokines, cells were stimulated for 4 h at 37°C in complete T cell media (IMDM with 10% FBS, 2 mM L-glutamine, 1 mM sodium pyruvate, 1× non-essential amino acids, and 1× antibiotic-antimycotic) supplemented with PMA/ionomycin cell stimulation cocktail (eBioscience) and 1× brefeldin A (eBioscience). Cells were incubated with Zombie NIR (BioLegend) Fixable Viability Kits diluted 1:500 in PBS for 15 min at 4°C. Samples were centrifuged, resuspended in FACS buffer with anti-CD16/32 (FC block; BioLegend), diluted 1:50 in FACS buffer,

and fluorescently conjugated antibodies were added for 20 min at 4°C. Cells were then fixed/permeabilized with Foxp3/Transcription Factor Staining Buffer Set (eBioscience) and stained for 10 min at room temperature with fluorescently conjugated antibodies against intracellular antigens. Following intracellular staining, samples were washed in FACS buffer, ran on a Cytek Aurora spectral flow cytometer (Cytek), and analyzed using FlowJo software (Tree Star).

FACS

For FACS of 10X Genomics scRNA-seq and plate-based FACS-seq, single-cell suspensions were prepared from the meninges and surface staining was performed as aforementioned, with the exception that cells were incubated with DAPI (0.2 mg/ml) rather than fixable viability dyes for discrimination of dead cells. For whole-dura scRNA-seq via the 10X platform, previously described, cells were sorted using the FACsAria II (BD Biosciences) into 1% BSA-coated 1.5 ml Eppendorf tubes with 500 ml of DMEM. For FACS-seq of meningeal LECs, individual LECs were sorted into 96-well plates containing 2 μl of 10X RNA lysis buffer (Takara) and 5% RNAse out (Takara) and were rapidly frozen over dry ice.

Whole dura scRNA-seq

scRNA-seq analysis of the dural meninges was performed on samples previously described (Rustenhoven et al., 2021). Briefly, a single-cell suspension was generated from five individual young and old dura per experiment, two experiments, 10 dura samples per age in total. Samples were stained with DAPI and sorted using a BD FACSAria II (BD Biosciences). Cells were sorted as DAPI⁻ singlets into 1.5-ml tubes with DMEM, pelleted, viability was determined using trypan blue exclusion, and they were resuspended in 0.04% non-acetylated BSA. The sorted young and old dural samples were loaded onto a 10X Genomics Chromium platform for Gel Bead-in-Emulsion and cDNA generation carrying cell- and transcript-specific barcodes, and sequencing libraries were constructed using the Chromium Single Cell 3′ Library & Gel Bead Kit v3. Libraries were sequenced on the Illumina NovaSeq6000, targeting a depth of 100,000 reads per cell.

Data preprocessing

Reads were aligned to the mm10 transcriptome using the Cell-ranger software pipeline (version 4.0) provided by 10X Genomics. The resulting filtered gene by cell matrices of UMI counts for each sample was read into R using the read10xCounts function from the Droplet Utils package. Filtering was applied to remove low-quality cells by excluding cells expressing <200 or >600 unique genes, having <1,500 or >50,000 UMI counts, as well as cells with >25% mitochondrial gene expression. Expression values for the remaining cells were then merged by gene symbol into one dataframe and normalized using the scran and scater packages. The resulting log₂ values were transformed to the natural log scale for compatibility with the Seurat (v3) pipeline.

Dimensionality reduction and clustering

The filtered and normalized matrix was used as input to the Seurat pipeline and cells were scaled across each gene before the

selection of the top 2,000 most highly variable genes using variance stabilizing transformation. Principal component analysis was conducted and an elbow plot was used to select the first 10 principal components for t-SNE analysis and clustering. Shared nearest neighbor clustering optimized with the Louvain algorithm, as implemented by the Seurat FindClusters function, was performed before manual annotation of clusters based on expression of canonical gene markers. Clusters were then collapsed based on common cell types to result in 17 clusters.

FACS-seq

For FACS-seq of meningeal LECs, dural meninges from five young (2–3 mo) and five old (20–24 mo) mice were peeled from the skull and processed into single-cell suspensions as previously described. FACS was performed using an Aria II and one cell per well of DAPI⁻ CD45⁻ CD31⁺ PDPN⁺ Lyve1⁺ cells were sorted into 96-well plates containing 2 µl of 10X RNA lysis buffer (Takara) and 5% RNAse out (Takara) and rapidly frozen over dry ice.

Library preparation was performed with 2 µl of single-cell lysates arrayed in 96-well PCR plates. Double-stranded cDNA (ds-cDNA) was prepared using a protocol adapted from the Takara-Clontech SMARTer methods and scaled to a 5 µl reaction volume. This method introduces a unique barcode upstream of the polyA tail using a modified oligo-dT primer. Briefly, 0.5 µl of the Takara dilution buffer with 5% RNase inhibitor and 0.25 µl of 25 µM FACSseq barcode primer were added to the lysate and heated to 72°C for 3 min. Then, 2.25 µl of the reverse transcription master mix was added to each well with 1 µl 5× first strand buffer, 0.125 µl 100 mM dithiothreitol, 0.25 µl 20 mM deoxynucleoside triphosphates, 0.25 µl, 50 µM FACSseq template switch oligo (TSO) primer, 0.125 µL RNase inhibitor, and 0.5 µl SMARTscribe reverse transcriptase (Takara). The reaction was incubated at 42°C for 90 min, 70°C for 10 min, then a 4°C hold. All wells from the plate were then pooled and purified with Ampure XP beads (Beckman Coulter) with a 1× ratio. cDNA was eluted in 39 µl of water. cDNA was amplified using 5 µl 10× PCR buffer, 2 µl 10 mM deoxynucleoside triphosphates, 2 µl 12 µM FACSseq206TSO PCR primer, and 2 µl 50× Advantage 2 Polymerase (Takara). PCR conditions were 95°C for 1 min, 16 cycles of 95°C for 15 s, 65°C for 30 s, 68°C for 6 min, 1 cycle of 72°C for 10 min, followed by a 4°C hold. cDNA was purified with 1.2× Ampure bead cleanup, measured with 209 Qubit dsDNA assay, and visualized on a bioanalyzer. cDNA was fragmented using a Covaris E220 210 sonicator using peak incident power 18, duty factor 20%, and cycles per burst 50 for 120 s. cDNA was blunt-ended, had an A base added to the 3′ ends, and had Illumina sequencing adapters ligated to the ends. Ligated fragments were then amplified for 16 cycles using a standard Illumina i7 primer to introduce an index sequence and FACS-seq Lib PCR 1.0 specific to fragments containing the cell barcode added during cDNA synthesis. Fragments were sequenced on an Illumina NextSeq using paired-end reads with 25 cycles for read 1, 7 cycles for the i7 index, and 100 cycles for the paired read. The sequencing run was performed with a custom sequencing primer for read 1 to read the 10 bp barcode unique to each cell. The i7 index allows for multiple plates to be sequenced together. Read 2 contains the mRNA sequences (Table 1).

FACS-seq analysis
Preprocessing and visualization

Sequencing was demultiplexed with a custom Python and Perl script and then aligned to the Ensembl release 76 top-level assembly with STAR version 2.5.1a. Gene counts were derived from the number of uniquely aligned unambiguous reads by Subread:featureCount version 1.4.6-p5. Further analysis was performed in R. First, cells were filtered to remove any that were three standard deviations outside the mean for either total features or total reads. This resulted in the exclusion of 27 cells leaving 357 for further analysis. Cells were normalized using Seurat's *SCTransform* function, regressing out total reads, total features, and percent mitochondria. Principal component analysis was conducted, and an elbow plot was used to select the first 11 principal components for t-SNE visualization.

Differential expression and pathway enrichment

For analysis of DEGs between conditions, each cluster was filtered to include genes that had at least five transcripts in at least five cells, then the top 2,000 highly variable genes were determined and included for further analysis using the SingleCellExperiment *modelGeneVar* and *getTopHVGs* functions. After filtering, observational weights for each gene were calculated using the ZINB-WaVE *zinbFit* and *zinbwave* functions (Van den Berge et al., 2018). These were then included in the edgeR model, which was created with the *glmFit* function, by using the *glmWeightedF* function (Robinson et al., 2010). Results were then filtered using a Benjamini–Hochberg adjusted P value threshold of <0.05 as statistically significant. Over-representation enrichment analysis with Fisher's exact test was used to determine significantly enriched GO terms (adjusted P < 0.05) for the sets of significantly DEGs. For each gene set, genes were separated into up- and downregulated, and (Hong et al., 2013) the *enrichGO* function from the clusterProfiler package was used separately with a gene set size set between 10 and 500 genes, and P values adjusted using the Benjamini–Hochberg correction (Yu et al., 2012).

IFNγ scoring

A signature was created by selecting genes from the bulk RNA-seq data described below with a log fold change >4 in IFNγ- vs. PBS-treated cells (136 genes in total), and then scoring assigned to FACS-seq LECs with Seurat's *AddModuleScore* function.

In vitro murine LEC culture

C57BL/6 mouse primary LECs were purchased from Cell Biologics. Cells were maintained in T25 tissue culture flasks with gelatin-based coating solution (Cell Biologics) and Complete Human Endothelial Cell Medium (Cell Biologics). Cells were passaged with Trypsin/EDTA 0.25% Solution (Cell Biolgics) and plated at 15,000 cells/cm² surface area in coated 6-well plates or 6-well chamber slides. Cells were grown ~72–96 h until a confluent monolayer was formed. For cytokine treatments, cells were treated every 24 h with vehicle (sterile PBS) or mouse IFNγ (5 ng/ml; R&D Systems) for 72 h. For antibody treatments, cells were treated for 6 h with 50 µg/ml CD144 (VE-Cadherin) clone BV13 (Invitrogen) or Rat IgG1 K isotype control (Invitrogen). For

Rustenhoven et al.
Aged meningeal immunity drives lymphatic impairments

Journal of Experimental Medicine   8 of 12
https://doi.org/10.1084/jem.20221929

Table 1. Oligo sequences for FACS-seq analysis

Oligos	Oligo sequence (5′–3′)
FACS-seq barcode[a]	AAGCAGTGGTATCAACGCAGAGTACXXXXXXXXXXTTTTT TTTTTTTTTTTTTTTTTTTTTTTTTVN
FACS-seq TSO	TSOAAGCAGTGGTATCAACGCAGAGTGAATrGrGrG
FACS-seq TSO PCR	PCRAAGCAGTGGTATCAACGCAGAGT
FACS-seq lib PCR 1.0	AATGATACGGCGACCACCGAGATCTACACGCCTGTCCGCGGAAGCAGTGGTATCAACGCAGAGT*A*CFACSseq
FACS-seq Custom Read1	GCCTGTCCGCGGAAGCAGTGGTATCAACGCAGAGTAC

[a]10 Xs in the FACS-seq barcode primer indicate a 10-nt barcode made up of unique sequences for each sample to be pooled.

immunocytochemistry, at completion, cells were fixed with 4% PFA for 15 min at room temperature, blocked/permeabilized with immunobuffer, and immunostained at 4°C overnight in an immunobuffer with primary antibodies and gentle agitation, washed in immunobuffer, and if required, stained for 2 h at room temperature with secondary antibodies in an immunobuffer. Cells were imaged using a Leica Stellaris confocal microscope or a Slideview VS200 (Olympus) wide-field fluorescent microscope. Image analysis was performed using FIJI software. For the determination of junctional disruption, a high-threshold parameter was applied to segment all cell boundaries and gaps between adjacent cells, which was determined as the percentage of area not covered by cells.

Bulk RNA-seq

For bulk RNA-seq of in vitro cultures, C57BL/6 mouse primary LECs were treated every 24 h with vehicle (sterile PBS) or mouse IFNγ (5 ng/ml; R&D Systems) for 72 h. At completion, RNA was extracted using the RNAqueous-Micro Total RNA Isolation Kit and DNAase was performed using the Invitrogen Ambion TURBO DNA free Kit. Total RNA integrity was determined using Agilent Bioanalyzer or 4200 Tapestation. Library preparation was performed with 500 ng of 1 µg of total RNA. Ribosomal RNA was removed by an RNase-H method using RiboErase kits (Kapa Biosystems). mRNA was then fragmented in reverse transcriptase buffer and heated to 94°C for 8 min. mRNA was reverse transcribed to yield cDNA using SuperScript III RT enzyme (Life Technologies, per the manufacturer's instructions) and random hexamers. A second strand reaction was performed to yield ds-cDNA. cDNA was blunt-ended, had an A base added to the 3′ ends, and then Illumina sequencing adapters ligated to the ends. Ligated fragments were then amplified for 12–15 cycles using primers incorporating unique dual index tags. Fragments were sequenced on an Illumina NovaSeq-6000 using paired-end reads extending 150 bases.

Bulk RNA-seq analysis

Basecalls and demultiplexing were performed with Illumina's bcl2fastq software with a maximum of one mismatch in the indexing read. Reads were then aligned to the Ensembl release 101 primary assembly with STAR version 2.7.9a1. Gene counts were derived from the number of uniquely aligned unambiguous reads by Subread:featureCount version 2.0.32. Gene counts were then read into R and analyzed with the edgeR package

(Robinson et al., 2010). Filtering out genes with low expression was done by excluding those with less than two counts per million. Normalization factors were calculated with calcNormFactors and then counts were normalized as log counts per million before undergoing principal component analysis via singular value decomposition. Raw counts were then used for differential expression analysis. Dispersion was estimated with estimateGLMRobustDisp to increase robustness against outliers and a quasi-likelihood model was fit with glmQLFit. Expression differential was tested with empirical Bayes quasi-likelihood F-test and results were then filtered using a Benjamini–Hochberg adjusted P value threshold of <0.05 as statistically significant. Genes matching this significance threshold were divided on the basis of up- or downregulation (Hong et al., 2013) and used as input for GO analysis using the clusterProfiler package (Yu et al., 2012).

In vitro human microfluidic cell culture

Human dermal lymphatic microvascular endothelial cells (CC-2543, HDLMEC) were enriched for LECs by FACS, immortalized as described previously (Wan et al., 2021), and transduced to express cytoplasmic GFP by using the LentiBrite GFP control lentiviral biosensor (EMD Millipore) following the vendor's protocol.

Cells were expanded in T75 flasks initially in Vasculife Endothelial Medium (LL-0003; Lifeline) supplemented with 8% FBS (Invitrogen) at 37°C and 5% CO_2. For the 3D microfluidic cultures, the same media supplemented with vascular endothelial growth factor-c (VEGF-C; R&D Systems), angiopoietin-1 (ANG-1; R&D Systems), and hepatocyte growth factor (HGF; Peprotech) were used at a 50 ng/ml concentration. 3D cell culture chips (idenTx 3 Chip; AIM Biotech) were filled with a 1:1 ratio of fibrinogen (cat. no. F8630-1G; Sigma-Aldrich, stock concentration 5 mg/ml in PBS) and thrombin (T4648-1KU; Sigma-Aldrich, 4 U/ml final thrombin solution diluted in basal media) to form the fibrin gel in the central region of the device by incubating the chips for 15 min at 37°C and 5% CO_2. Then the media channel side that will host the lymphatic cells was coated with human plasma fibronectin (EMD Millipore) at a concentration of 100 µg/ml for 45 min and then washed out. Cells were collected after washing with PBS and incubated for 5 min at 37°C and 5% CO_2 with TrypLE Express (Thermo Fisher Scientific). 30 µl of 3 × 10^6 cells/ml suspension were attached to the side of the gel that had previously been coated with the fibronectin by

Rustenhoven et al.
Aged meningeal immunity drives lymphatic impairments

Journal of Experimental Medicine 9 of 12
https://doi.org/10.1084/jem.20221929

tilting the device at 90° for 20 min at room temperature and then incubated at 37°C and 5% CO_2 overnight (day 0) with both media channels filled with media. The following day (day 1) a hydrostatic pressure difference across the fibrin gel of 3 cm H_2O was established by using luer connectors (AIM Biotech) to attach 3 ml syringes (BH Supplies) to the ports on the cell-free media channel side, creating an interstitial flow through the gel toward the lymphatic channel. Media were added daily to maintain the pressure difference for 5 d. For the IFNγ-treated samples, IFNγ (Peprotech) at 2 U/ml concentration was added on day 1 and changed daily as described previously for the non-treated samples. Imaging was performed using an Olympus FLUOVIEW FV1200 confocal laser scanning microscope with a 10× objective. On the imaging day (day 5) dextran, Texas Red 40,000 MW, Neutral (Thermo Fisher scientific) was introduced in the side of the syringes to create a 1 cm H_2O hydrostatic pressure difference and drive a physiological flow rate of ∼0.5–1.5 µm/s to measure solute drainage rates. Three to four regions of interest were selected (four to five slices ∼80 µm each to include the entire media channel) in the lymphatic media channel side, and z-stacks were acquired every 2 min. For normalization purposes, the same z-stack range was acquired in the cell-free media channel at the end of the experiment to get an average intensity value of the media channel that is fully filled with dextran throughout the experiment. Solute drainage rates were calculated according to

$$Solute\ Drainage\ Rate = \frac{\Delta I_v}{\Delta t}\frac{1}{I_s},$$

where ΔI_v indicates the increase in the average fluorescence intensity in the lymphatic media channel in a time interval Δt and I_s represents the average intensity in the cell free media channel.

For 2D experiments with VE-Cadherin, a similar approach was followed to that in the microfluidic devices. Media were changed daily, and cells were fixed on day 5 and stained for VE-Cadherin (Cell Signaling).

Quantification and statistical analysis

Statistical methods were not used to recalculate or predetermine study sizes but were based on similar experiments previously published (Rustenhoven et al., 2021; Cugurra et al., 2021; Mazzitelli et al., 2022). Experiments were blinded for at least one of the independent experiments. No data were excluded for analysis. For all experiments, animals from different cages were randomly assigned to different experimental groups. All in vivo experiments were replicated in at least two independent experiments, and all replication was successful. Statistical tests for each experiment are provided in the respective figure legends. Statistical analysis was performed using Prism (version 8.0, GraphPad Software).

Online supplemental material

Fig. S1 shows the phenotyping of young and aged meningeal T cells and the determination of IFNγ-mediated glymphatic function. Fig. S2 shows the examination of the VEGF-A-VEGFR2 signaling in the aged meninges. Fig. S3 shows the IFNγ response signature in aged meningeal LECs and characterization of 3D microfluidic models and IFNγ-mediated junctional disruption in human LECs.

Data availability

The data underlying Figs. 1, 2, and 3 are available in the published article and its online supplemental material. The data underlying Fig. 1, B–E; Fig. S2, D and E; and Fig. S3, B–E are openly available in the Gene Expression Omnibus under accession number GSE217314. The data underlying Fig. 1, F–H; Fig. S1, A–E; and Fig. S2, A–C are openly available in the Gene Expression Omnibus under the accession number GSE161290. These data were derived from sources in the public domain, specifically Rustenhoven et al. (2021). All codes used to analyze single and bulk RNA-seq are available from authors upon reasonable request.

References

Absinta, M., S.-K. Ha, G. Nair, P. Sati, N.J. Luciano, M. Palisoc, A. Louveau, K.A. Zaghloul, S. Pittaluga, J. Kipnis, and D.S. Reich. 2017. Human and nonhuman primate meninges harbor lymphatic vessels that can be visualized noninvasively by MRI. *Elife.* 6:e29738. https://doi.org/10.7554/eLife.29738

Ahn, J.H., H. Cho, J.-H. Kim, S.H. Kim, J.-S. Ham, I. Park, S.H. Suh, S.P. Hong, J.-H. Song, Y.-K. Hong, et al. 2019. Meningeal lymphatic vessels at the skull base drain cerebrospinal fluid. *Nature.* 572:62–66. https://doi.org/10.1038/s41586-019-1419-5

Alves de Lima, K., J. Rustenhoven, S. Da Mesquita, M. Wall, A.F. Salvador, I. Smirnov, G. Martelossi Cebinelli, T. Mamuladze, W. Baker, Z. Papadopoulos, et al. 2020a. Meningeal γδ T cells regulate anxiety-like behavior via IL-17a signaling in neurons. *Nat. Immunol.* 21:1421–1429. https://doi.org/10.1038/s41590-020-0776-4

Alves de Lima, K., J. Rustenhoven, and J. Kipnis. 2020b. Meningeal immunity and its function in maintenance of the central nervous system in health and disease. *Annu. Rev. Immunol.* 38:597–620. https://doi.org/10.1146/annurev-immunol-102319-103410

Antila, S., S. Karaman, H. Nurmi, M. Airavaara, M.H. Voutilainen, T. Mathivet, D. Chilov, Z. Li, T. Koppinen, J.-H. Park, et al. 2017. Development and plasticity of meningeal lymphatic vessels. *J. Exp. Med.* 214:3645–3667. https://doi.org/10.1084/jem.20170391

Aspelund, A., S. Antila, S.T. Proulx, T.V. Karlsen, S. Karaman, M. Detmar, H. Wiig, and K. Alitalo. 2015. A dural lymphatic vascular system that drains brain interstitial fluid and macromolecules. *J. Exp. Med.* 212:991–999. https://doi.org/10.1084/jem.20142290

Benveniste, H., X. Liu, S. Koundal, S. Sanggaard, H. Lee, and J. Wardlaw. 2019. The glymphatic system and waste clearance with brain aging: A review. *Gerontology.* 65:106–119. https://doi.org/10.1159/000490349

Boland, B., W.H. Yu, O. Corti, B. Mollereau, A. Henriques, E. Bezard, G.M. Pastores, D.C. Rubinsztein, R.A. Nixon, M.R. Duchen, et al. 2018. Promoting the clearance of neurotoxic proteins in neurodegenerative disorders of ageing. *Nat. Rev. Drug Discov.* 17:660–688. https://doi.org/10.1038/nrd.2018.109

Churchill, M.J., H. du Bois, T.A. Heim, T. Mudianto, M.M. Steele, J.C. Nolz, and A.W. Lund. 2022. Infection-induced lymphatic zippering restricts fluid transport and viral dissemination from skin. *J. Exp. Med.* 219:e20211830. https://doi.org/10.1084/jem.20211830

Corada, M., M. Mariotti, G. Thurston, K. Smith, R. Kunkel, M. Brockhaus, M.G. Lampugnani, I. Martin-Padura, A. Stoppacciaro, L. Ruco, et al. 1999. Vascular endothelial-cadherin is an important determinant of microvascular integrity in vivo. *Proc. Natl. Acad. Sci. USA.* 96:9815–9820. https://doi.org/10.1073/pnas.96.17.9815

Cugurra, A., T. Mamuladze, J. Rustenhoven, T. Dykstra, G. Beroshvili, Z.J. Greenberg, W. Baker, Z. Papadopoulos, A. Drieu, S. Blackburn, et al. 2021. Skull and vertebral bone marrow are myeloid cell reservoirs for the meninges and CNS parenchyma. *Science.* 373:eabf7844. https://doi.org/10.1126/science.abf7844

Da Mesquita, S., A. Louveau, A. Vaccari, I. Smirnov, R.C. Cornelison, K.M. Kingsmore, C. Contarino, S. Onengut-Gumuscu, E. Farber, D. Raper, et al. 2018. Functional aspects of meningeal lymphatics in ageing and Alzheimer's disease. *Nature.* 560:185–191. https://doi.org/10.1038/s41586-018-0368-8

Da Mesquita, S., Z. Papadopoulos, T. Dykstra, L. Brase, F.G. Farias, M. Wall, H. Jiang, C.D. Kodira, K. Alves de Lima, J. Herz, et al. 2021. Meningeal lymphatics affect microglia responses and anti-Aβ immunotherapy. *Nature.* 593:255–260. https://doi.org/10.1038/s41586-021-03489-0

Ding, X.-B., X.-X. Wang, D.-H. Xia, H. Liu, H.-Y. Tian, Y. Fu, Y.-K. Chen, C. Qin, J.-Q. Wang, Z. Xiang, et al. 2021. Impaired meningeal lymphatic drainage in patients with idiopathic Parkinson's disease. *Nat. Med.* 27:411–418. https://doi.org/10.1038/s41591-020-01198-1

Filiano, A.J., Y. Xu, N.J. Tustison, R.L. Marsh, W. Baker, I. Smirnov, C.C. Overall, S.P. Gadani, S.D. Turner, Z. Weng, et al. 2016. Unexpected role of interferon-γ in regulating neuronal connectivity and social behaviour. *Nature.* 535:425–429. https://doi.org/10.1038/nature18626

Hägerling, R., E. Hoppe, C. Dierkes, M. Stehling, T. Makinen, S. Butz, D. Vestweber, and F. Kiefer. 2018. Distinct roles of VE-cadherin for development and maintenance of specific lymph vessel beds. *EMBO J.* 37:e98271. https://doi.org/10.15252/embj.201798271

Herz, J., Z. Fu, K. Kim, T. Dykstra, M. Wall, H. Li, A.F. Salvador, B. Zou, N. Yan, S.M. Blackburn, et al. 2021. GABAergic neuronal IL-4R mediates T cell effect on memory. *Neuron.* 109:3609–3618.e9. https://doi.org/10.1016/j.neuron.2021.10.022

Hong, G., W. Zhang, H. Li, X. Shen, and Z. Guo. 2013. Separate enrichment analysis of pathways for up- and downregulated genes. *J. R. Soc. Interf.* 11:20130950. https://doi.org/10.1098/rsif.2013.0950

Hou, Y., X. Dan, M. Babbar, Y. Wei, S.G. Hasselbalch, D.L. Croteau, and V.A. Bohr. 2019. Ageing as a risk factor for neurodegenerative disease. *Nat. Rev. Neurol.* 15:565–581. https://doi.org/10.1038/s41582-019-0244-7

Iliff, J.J., M. Wang, Y. Liao, B.A. Plogg, W. Peng, G.A. Gundersen, H. Benveniste, G.E. Vates, R. Deane, S.A. Goldman, et al. 2012. A paravascular pathway facilitates CSF flow through the brain parenchyma and the clearance of interstitial solutes, including amyloid β. *Sci. Transl. Med.* 4:147ra111. https://doi.org/10.1126/scitranslmed.3003748

Jannaway, M., and J.P. Scallan. 2021. VE-cadherin and vesicles differentially regulate lymphatic vascular permeability to solutes of various sizes. *Front. Physiol.* 12:687563. https://doi.org/10.3389/fphys.2021.687563

Kataru, R.P., H. Kim, C. Jang, D.K. Choi, B.I. Koh, M. Kim, S. Gollamudi, Y.-K. Kim, S.-H. Lee, and G.Y. Koh. 2011. T lymphocytes negatively regulate lymph node lymphatic vessel formation. *Immunity.* 34:96–107. https://doi.org/10.1016/j.immuni.2010.12.016

Kress, B.T., J.J. Iliff, M. Xia, M. Wang, H.S. Wei, D. Zeppenfeld, L. Xie, H. Kang, Q. Xu, J.A. Liew, et al. 2014. Impairment of paravascular clearance pathways in the aging brain. *Ann. Neurol.* 76:845–861. https://doi.org/10.1002/ana.24271

Louveau, A., J. Herz, M.N. Alme, A.F. Salvador, M.Q. Dong, K.E. Viar, S.G. Herod, J. Knopp, J.C. Setliff, A.L. Lupi, et al. 2018. CNS lymphatic drainage and neuroinflammation are regulated by meningeal lymphatic vasculature. *Nat. Neurosci.* 21:1380–1391. https://doi.org/10.1038/s41593-018-0227-9

Louveau, A., B.A. Plog, S. Antila, K. Alitalo, M. Nedergaard, and J. Kipnis. 2017. Understanding the functions and relationships of the glymphatic system and meningeal lymphatics. *J. Clin. Invest.* 127:3210–3219. https://doi.org/10.1172/JCI90603

Louveau, A., I. Smirnov, T.J. Keyes, J.D. Eccles, S.J. Rouhani, J.D. Peske, N.C. Derecki, D. Castle, J.W. Mandell, K.S. Lee, et al. 2015. Structural and functional features of central nervous system lymphatic vessels. *Nature.* 523:337–341. https://doi.org/10.1038/nature14432

Mazzitelli, J.A., L.C.D. Smyth, K.A. Cross, T. Dykstra, J. Sun, S. Du, T. Mamuladze, I. Smirnov, J. Rustenhoven, and J. Kipnis. 2022. Cerebrospinal fluid regulates skull bone marrow niches via direct access through dural channels. *Nat. Neurosci.* 25:555–560. https://doi.org/10.1038/s41593-022-01029-1

Mrdjen, D., A. Pavlovic, F.J. Hartmann, B. Schreiner, S.G. Utz, B.P. Leung, I. Lelios, F.L. Heppner, J. Kipnis, D. Merkler, et al. 2018. High-dimensional single-cell mapping of central nervous system immune cells reveals distinct myeloid subsets in Health, aging, and disease. *Immunity.* 48:380–395.e6. https://doi.org/10.1016/j.immuni.2018.01.011

Oliver, G., J. Kipnis, G.J. Randolph, and N.L. Harvey. 2020. The lymphatic vasculature in the 21st century: Novel functional roles in homeostasis and disease. *Cell.* 182:270–296. https://doi.org/10.1016/j.cell.2020.06.039

Patel, T.K., L. Habimana-Griffin, X. Gao, B. Xu, S. Achilefu, K. Alitalo, C.A. McKee, P.W. Sheehan, E.S. Musiek, C. Xiong, et al. 2019. Dural lymphatics regulate clearance of extracellular tau from the CNS. *Mol. Neurodegener.* 14:11. https://doi.org/10.1186/s13024-019-0312-x

Ringstad, G., and P.K. Eide. 2020. Cerebrospinal fluid tracer efflux to parasagittal dura in humans. *Nat. Commun.* 11:354. https://doi.org/10.1038/s41467-019-14195-x

Robinson, M.D., D.J. McCarthy, and G.K. Smyth. 2010. edgeR: A Bioconductor package for differential expression analysis of digital gene expression data. *Bioinformatics.* 26:139–140. https://doi.org/10.1093/bioinformatics/btp616

Roth, T.L., D. Nayak, T. Atanasijevic, A.P. Koretsky, L.L. Latour, and D.B. McGavern. 2014. Transcranial amelioration of inflammation and cell death after brain injury. *Nature.* 505:223–228. https://doi.org/10.1038/nature12808

Rustenhoven, J., A. Drieu, T. Mamuladze, K.A. de Lima, T. Dykstra, M. Wall, Z. Papadopoulos, M. Kanamori, A.F. Salvador, W. Baker, et al. 2021. Functional characterization of the dural sinuses as a neuroimmune interface. *Cell.* 184:1000–1016.e27. https://doi.org/10.1016/j.cell.2020.12.040

Salvador, A.F., K.A. de Lima, and J. Kipnis. 2021. Neuromodulation by the immune system: A focus on cytokines. *Nat. Rev. Immunol.* 21:526–541. https://doi.org/10.1038/s41577-021-00508-z

Shin, K., R.P. Kataru, H.J. Park, B.-I. Kwon, T.W. Kim, Y.K. Hong, and S.-H. Lee. 2015. TH2 cells and their cytokines regulate formation and function of lymphatic vessels. *Nat. Commun.* 6:6196. https://doi.org/10.1038/ncomms7196

Van den Berge, K., F. Perraudeau, C. Soneson, M.I. Love, D. Risso, J.-P. Vert, M.D. Robinson, S. Dudoit, and L. Clement. 2018. Observation weights unlock bulk RNA-seq tools for zero inflation and single-cell applications. *Genome Biol.* 19:24. https://doi.org/10.1186/s13059-018-1406-4

Van Hove, H., L. Martens, I. Scheyltjens, K. De Vlaminck, A.R. Pombo Antunes, S. De Prijck, N. Vandamme, S. De Schepper, G. Van Isterdael, C.L. Scott, et al. 2019. A single-cell atlas of mouse brain macrophages reveals unique transcriptional identities shaped by ontogeny and tissue environment. *Nat. Neurosci.* 22:1021–1035. https://doi.org/10.1038/s41593-019-0393-4

Wan, Z., S. Zhang, A.X. Zhong, S.E. Shelton, M. Campisi, S.K. Sundararaman, G.S. Offeddu, E. Ko, L. Ibrahim, M.F. Coughlin, et al. 2021. A robust vasculogenic microfluidic model using human immortalized endothelial cells and Thy1 positive fibroblasts. *Biomaterials.* 276:121032. https://doi.org/10.1016/j.biomaterials.2021.121032

Yang, Y., B. Cha, Z.Y. Motawe, R.S. Srinivasan, and J.P. Scallan. 2019. VE-cadherin is required for lymphatic valve formation and maintenance. *Cell Rep.* 28:2397–2412.e4. https://doi.org/10.1016/j.celrep.2019.07.072

Yu, G., L.-G. Wang, Y. Han, and Q.-Y. He. 2012. clusterProfiler: An R package for comparing biological themes among gene clusters. *Omics J. Integr. Biol.* 16:284–287. https://doi.org/10.1089/omi.2011.0118

Zlokovic, B.V. 2005. Neurovascular mechanisms of Alzheimer's neurodegeneration. *Trends Neurosci.* 28:202–208. https://doi.org/10.1016/j.tins.2005.02.001

Zou, W., T. Pu, W. Feng, M. Lu, Y. Zheng, R. Du, M. Xiao, and G. Hu. 2019. Blocking meningeal lymphatic drainage aggravates Parkinson's disease-like pathology in mice overexpressing mutated α-synuclein. *Transl. Neurodegener.* 8:7. https://doi.org/10.1186/s40035-019-0147-y
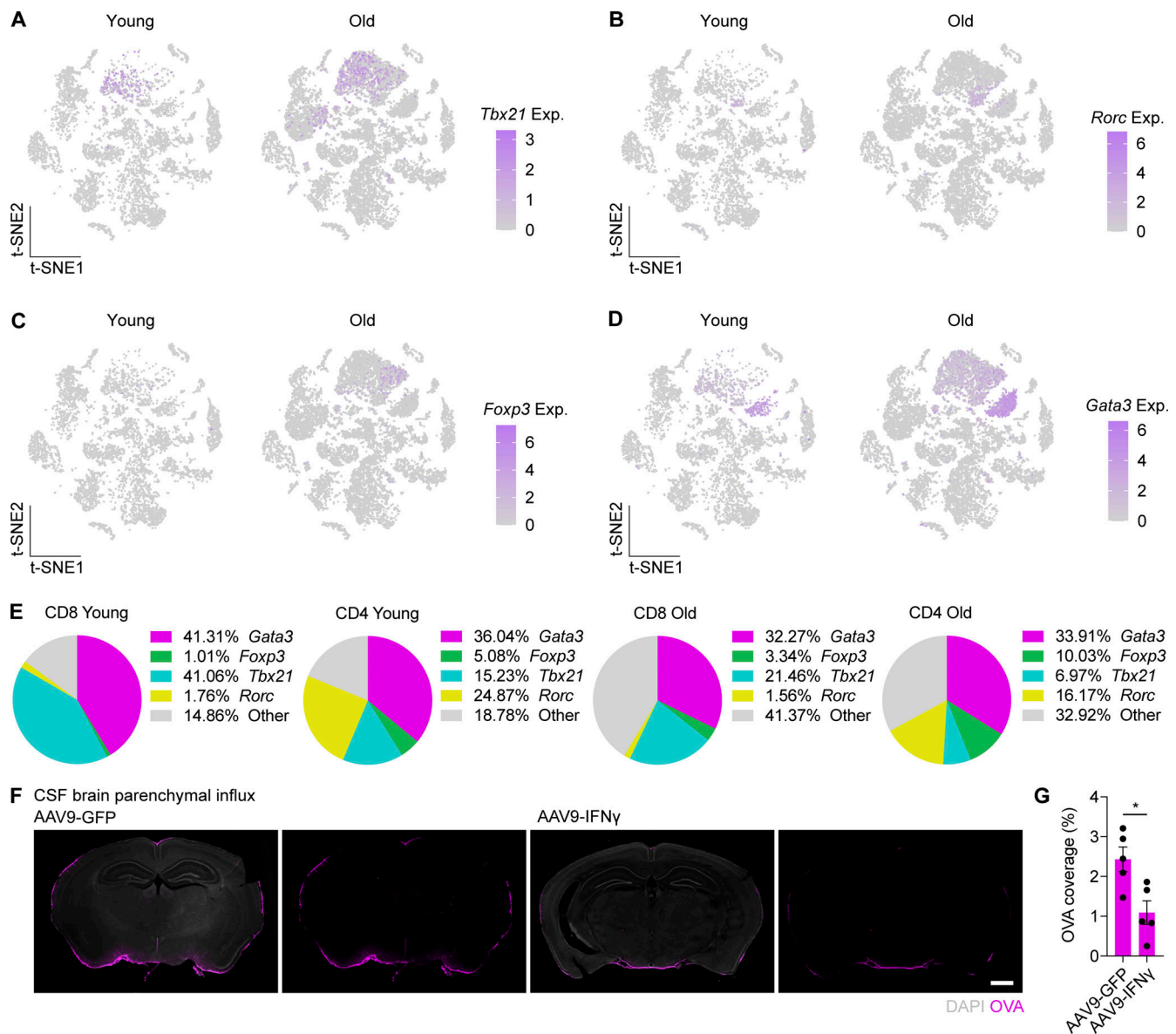
Supplemental material

Figure S1. **Phenotyping young and aged meningeal T cells and determination of IFNγ -mediated glymphatic function. (A–D)** t-SNE visualization of scRNA-seq of cells isolated from young (2–3 mo) and aged (20–24 mo) mouse dura. Data are from Rustenhoven et al. (2021). Expression of *Tbx21, Rorc, Foxp3,* and *Gata3* is shown. *n* = 5 individual young and old dura per experiment, *n* = 2 independent experiments, 10 dura samples per age total. **(E)** Pie charts demonstrating the percentage of CD4 or CD8 T cells in young and aged mice expressing *Tbx21, Rorc, Foxp3,* and *Gata3* from sequencing analysis. **(F and G)** Immunohistochemistry and quantification of OVA-594 coverage in the brains of mice that received an i.c.m. injection of 2 μl of 1 × 10^13 GC of AAV9-CCMV-GFP or AAV9-CCMV-IFNγ at 2 mo of age, and an i.c.m. injection of 2.5 μl OVA-594 (1 μg/μl) 1 h prior to sacrifice at 3 mo of age. *, P < 0.05 (Student's *t* test), *n* = 5 individual mice per experiment, representative of *n* = 2 independent experiments. Scale bar = 1 mm.
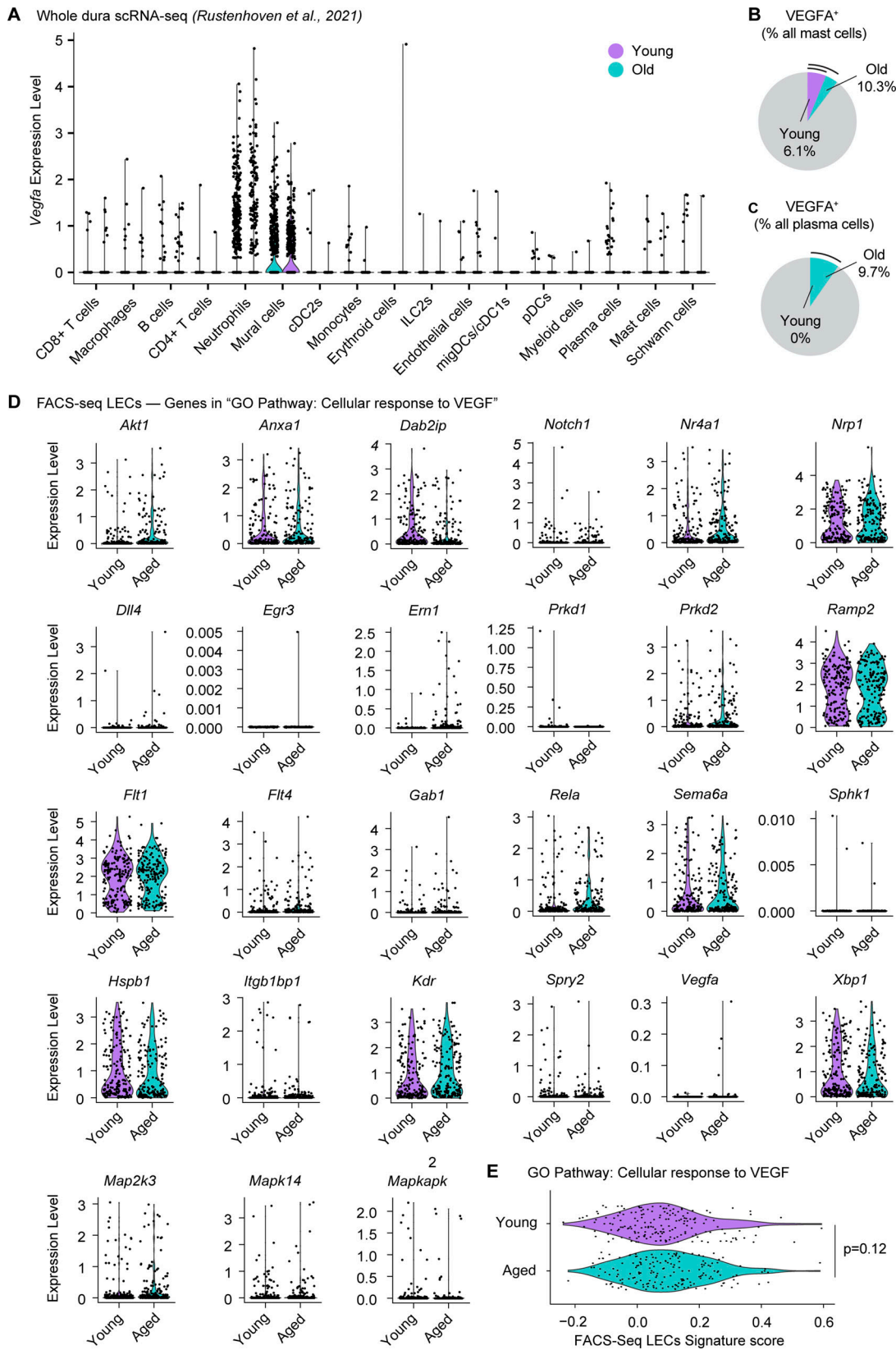
Figure S2. VEGF-A-VEGFR2 signaling in the aged meninges. (A) Violin plot demonstrating *Vegfa* gene expression in meningeal cells of young and aged mice. **(B and C)** Pie chart demonstrating *Vegfa*+ mast cells and plasma cells as a percentage of their respective cell cluster in young and aged mice from sequencing analysis. **(D)** Violin plots demonstrating individual genes present in the "Cellular response to VEGF" GO pathway expression in young and aged meningeal LECs from FACS-seq analysis. **(E)** FACS-seq LEC signature score for overall cellular response to VEGF GO pathway expression in young and aged LECs (Mann–Whitney U test), *n* = 5 individual young and old dura per experiment, *n* = 2 independent experiments, 10 dura samples per age total.
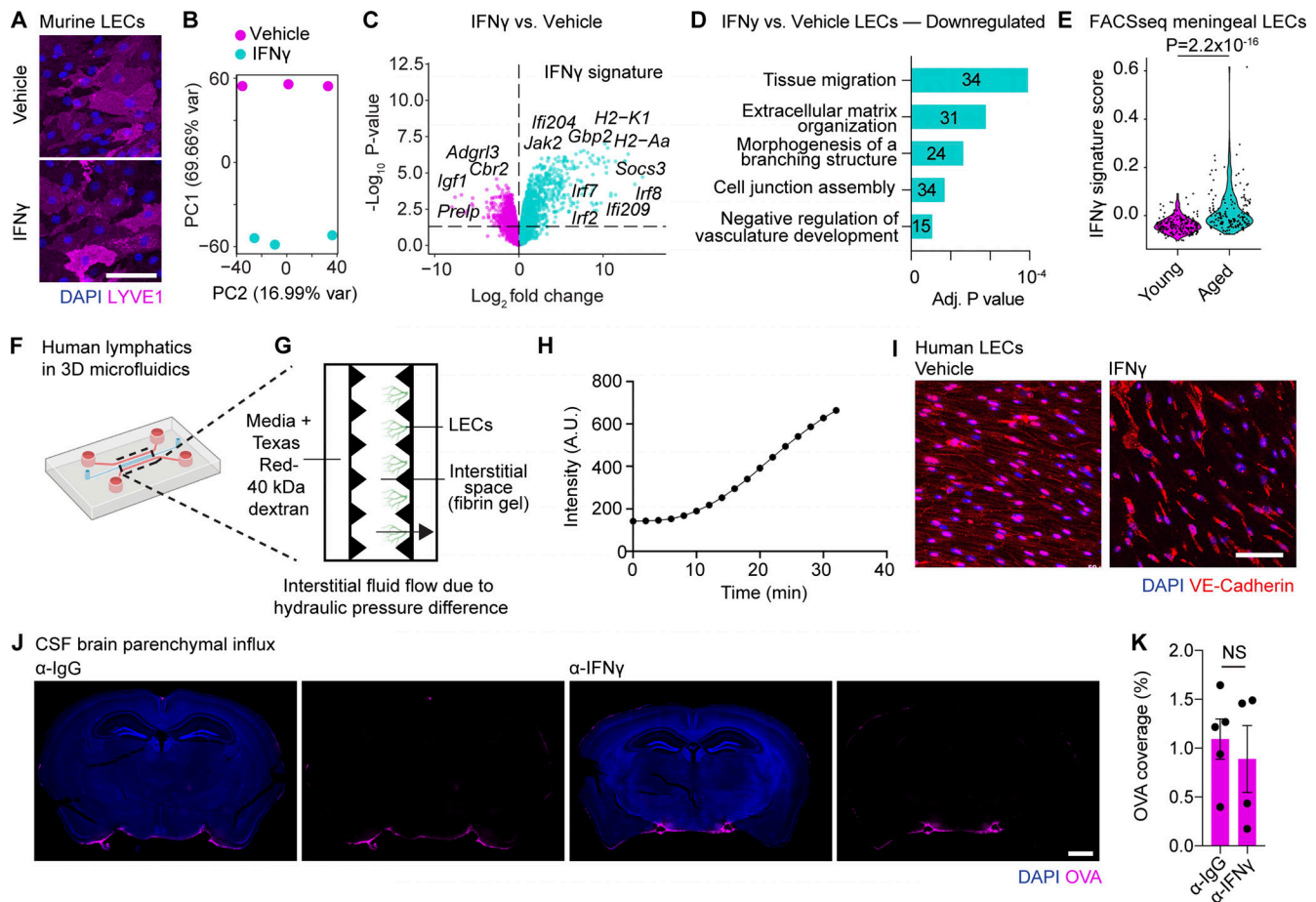
Figure S3. **IFNγ response signature in aged meningeal LECs and characterization of 3D microfluidic models and IFNγ-mediated junctional disruption in human LECs. (A)** Immunocytochemistry of LYVE1 expression in C57BL/6 mouse primary dermal LECs treated every 24 h for 72 h with 5 ng/ml IFNγ or a vehicle control. Scale bar = 50 µm. **(B and C)** Principal component analysis plot and volcano plot of RNA-seq analysis for C57BL/6 mouse primary dermal LECs treated every 24 h for 72 h with 5 ng/ml IFNγ or a vehicle control, n = 3 independent experiments. **(D)** GO pathway analysis demonstrating enriched pathways downregulated in IFNγ-treated LECs. Numbers represent the number of genes in respective pathways. **(E)** Violin plot demonstrating the IFNγ signature score in young and old meningeal LECS (Mann–Whitney U test), n = 5 individual young and old dura per experiment, n = 2 independent experiments, 10 dura samples per age total. **(F and G)** Schematic of 3D microfluidic devices used to study lymphatic function. Human LECs were cultured in 3D fibrin matrices on-chip to form luminized sprouts. Media is supplied by lateral chambers and interstitial solutes are administered via central chambers which are drained via lymphatic vasculature due to hydraulic pressure differences. **(H)** Example quantification of solute drainage rate over time, demonstrated by increased fluorescence intensity in the interstitial space determined by imaging snapshots of 40 kD drainage using 3D microfluidic devices. Data representative of n = 3 individual devices **(I)**. Immunocytochemistry of VE-Cadherin in human primary dermal LECs treated for 5 d every 24 h with 2 U/ml IFNγ or a vehicle control, representative of n = 2 independent experiments. Scale bar = 100 µm. **(J and K)** Immunohistochemistry and quantification of OVA-594 coverage in the brains of aged mice that received i.p. injections of 200 µg anti-IgG or anti-IFNγ every 72 h for 8 wk and an i.c.m. injection of 2.5 µl OVA-594 (1 µg/µl) 1 h prior to sacrifice at 3 mo of age. NS, P > 0.05 (Student's t test), n = 4–5 individual mice per experiment, representative of n = 2 independent experiments. Scale bar = 1 mm.